J. Fluid Mech. (2008), *vol.* 613, *pp.* 205–231.
doi:10.1017/S0022112008003005 Printed in the United Kingdom

Characterization of coherent vortical structures in a supersonic turbulent boundary layer

SERGIO PIROZZOLI, MATTEO BERNARDINI AND FRANCESCO GRASSO

Dipartimento di Meccanica e Aeronautica, Università di Roma 'La Sapienza', Via Eudossiana 18, 00184 Roma, Italy

(Received 17 September 2007 and in revised form 13 June 2008)

A spatially developing supersonic boundary layer at Mach 2 is analysed by means of direct numerical simulation of the compressible Navier–Stokes equations, with the objective of quantitatively characterizing the coherent vortical structures. The study shows structural similarities with the incompressible case. In particular, the inner layer is mainly populated by quasi-streamwise vortices, while in the outer layer we observe a large variety of structures, including hairpin vortices and hairpin packets. The characteristic properties of the educed structures are found to be nearly uniform throughout the outer layer, and to be weakly affected by the local vortex orientation. In the outer layer, typical core radii vary in the range of 5–6 dissipative length scales, and the associated circulation is approximately constant, and of the order of 180 wall units. The statistical properties of the vortical structures in the outer layer are similar to those of an ensemble of non-interacting closed-loop vortices with a nearly planar head inclined at an angle of approximately 20° with respect to the wall, and with an overall size of approximately 30 dissipative length scales.

1. Introduction

The importance of coherent eddy structures in turbulent wall-bounded flows has been recognized since the pioneering work of Theodorsen (1952), who proposed that incompressible turbulent boundary layers are populated by hairpin-like structures attached to the wall. These structures are responsible for transport of low-momentum fluid and for Reynolds-stress production, and are the main cause of ejections and sweeps. Townsend (1976) first observed that the turbulent motion in the constant-stress (logarithmic) region of the boundary layer can be explained by considering the existence of organized flow patterns that extend to the wall. These structures are self-similar and their characteristic scales vary with the wall distance, and in this respect they are 'attached' to the wall. Townsend's attached-eddy model was later exploited for quantitative predictions on the structure of the logarithmic layer by Perry & Chong (1982), who assumed that the wall layer is populated by randomly distributed hairpin-like vortices.

Early experimental works (Kim, Kline & Reynolds 1971; Kline *et al.* 1967; Head & Bandyopadhyay 1981) provided substantial support to the attached-eddy concept and showed the existence of low- and high-speed streaks in the inner part of the boundary layer, having a characteristic spacing of about 100 wall units in the spanwise direction and extending for approximately 1000 wall units in the streamwise direction. The numerical and experimental data reviewed by Robinson (1991*a*) provided evidence

for the existence of elongated vortices leaning in the forward streamwise direction at an angle that increases with distance from the wall.

The emergence of direct numerical simulations (DNS) and of more advanced experimental techniques have recently contributed to better elucidate the responsible mechanisms for the generation and interaction of the different vortical structures in wall-bounded turbulent flows. By using the DNS database of Spalart (1988), Chong *et al.* (1998) have characterized the topological properties of wall-bounded flows, and have confirmed the occurrence of Theodorsen's hairpin-like vortices, as well as the existence of vortex tubes nearly aligned with the streamwise direction. According to the mechanism proposed by Hamilton, Kim & Waleffe (1995), and supported by the numerical experiments of Jiménez & Pinelli (1999), near-wall turbulence is sustained by a closed-loop mechanism, whereby streaks are formed owing to advection of the mean velocity field by quasi-streamwise vortices (whose characteristic length is $O(100)$ wall units), which are in turn generated by streak instability. A fraction of the quasi-streamwise vortices coalesce owing to sustained stretching by mean shear, forming hairpin vortices that grow while moving downstream and become the most frequently observed structures in the outer part of the boundary layer (Hutchins, Hambleton & Marušić 2005; Ganapathisubramani, Longmire & Marušić 2006). An alternative mechanism for the sustainment of near-wall turbulence has been proposed by Chernyshenko & Baig (2005), whereby streaks are first formed owing to the pattern-forming properties of the combined action of wall-normal motions, mean shear and viscous diffusion.

In order to explain the apparent disparities in the observed length scales of the streaks and of the quasi-streamwise vortices, Adrian, Meinhart & Tomkins (2000) have provided evidence of the existence of vortex packets, which consist of several streamwise vortices and hairpins associated with the same streak. The numerical simulations of the evolution of an isolated hairpin vortex carried out by Zhou *et al.* (1999) have confirmed that trains of secondary hairpin vortices are generated, provided the strength of the parent structure exceeds a suitable threshold. Such a scenario is consistent with the experimental observations of Head & Bandyopadhyay (1981) and the more recent results of Ganapathisubramani *et al.* (2006). Del Álamo *et al.* (2006) have studied the organization of vortex clusters in the outer layer of a turbulent channel by means of DNS, and found that the population of vortices in the logarithmic layer naturally breaks into two families. The first one includes wall-detached vortices, which are distributed almost uniformly throughout the outer layer. The typical size of the wall-detached vortices is of the order of the Kolmogorov length scale (η), and it does not depend upon the distance from the wall. In particular, Del Álamo *et al.* (2006) found that the overall size of detached vortex clusters is $\Delta \simeq 20\,\eta$, and their core size is $4 \leqslant r_0/\eta \leqslant 6$. The second family consists of Townsend's wall-attached eddies, which grow self-similarly in time and closely resemble the large arrays of hairpins observed by Adrian *et al.* (2000), being responsible for the establishment of the mean shearing field. The number density of clusters of the second family is smaller than that associated with the first family; nevertheless, they are dynamically more relevant, their size being larger and their contribution to the production of the Reynolds stress more significant.

The geometric features (size and orientation) of coherent vortices in low-speed wall turbulence were first investigated by Blackwelder & Eckelmann (1979), who experimentally detected counter-rotating vortex pairs by means of conditional analysis. Those authors found the expected vortex centre at $y^+ \approx 15$ (in wall units), expected radius $r_0^+ \approx 15$, streamwise extent of 200^+ and spanwise spacing of

50^+ –200^+. Robinson (1991*b*) computed probability distributions of radii, circulations and wall distances for quasi-streamwise vortices based on the DNS database of Spalart (1988). His results showed that the number density of vortices peaks at about $y^+ \approx 10$–50, the most probable radius is in the range $r_0^+ \approx 5$–20, and the typical non-dimensional circulation is Γ^+ $(= \Gamma/\nu) \approx 60$–250. Carlier & Stanislas (2005) have carried out an experimental investigation whereby eddy structures are detected by means of a pattern-recognition algorithm and vortex parameters are determined by fitting the vortex cores with an Oseen model. Their results showed that in the range of Reynolds numbers investigated ($7500 \leqslant Re_\theta \leqslant 19\,000$), the eddy structures are organized as cane-shaped vortices tilted downstream at an angle close to 45°. The eddies have an apparent origin at $y^+ \approx 25$ and their size ($r_0^+ \approx 18$–25) increases with both the Reynolds number and the distance from the wall, while the circulation is approximately constant ($\Gamma^+ \approx 235$–250, M. Stanislas 2007, personal communication).

Ganapathisubramani *et al.* (2006) have performed dual-plane particle-image velocimetry (PIV) experiments of a low-speed turbulent boundary layer at $Re_\tau = 1160$ and studied the geometric orientation of vortex cores both in the logarithmic region (at $y^+ = 110$) and in the wake region (at $y/\delta = 0.53$). Their study reveals the occurrence of forward leaning vortex cores whose number density decreases with the wall-normal distance, and whose most probable elevation (the angle formed by the vortex with the wall plane) is 38° in the log layer and 33° in the wake region. Furthermore, the most probable eddy inclination angle (the angle made in the streamwise-wall-normal plane) is found to be approximately equal to 45° in both regions. Consistent with kinematic models based on the attached-eddy hypothesis (Perry & Marušić 1995; Marušić & Perry 1995), the study also indicates the presence of inward-leaning vortex cores and spanwise oriented cores.

While the structural features of low-speed boundary layers seem to be well understood, much less is known to date about the behaviour of their high-speed counterparts. In particular, the knowledge of the inner-layer dynamics of compressible boundary layers is limited to qualitative analysis of DNS data. As first suggested by Morkovin (1961), it is generally acknowledged that for supersonic flows with moderate Mach number, the direct effects of compressibility on wall turbulence at zero pressure gradient are small, the most notable differences being due to variations of the thermodynamic properties across the layer. All available experimental data (see Smits & Dussauge 2006 and references therein) confirm that supersonic boundary layers at zero pressure gradient exhibit close similarities with incompressible ones, and that the main turbulence statistics can be correctly predicted as variable-density extensions of incompressible results. Direct numerical simulations of zero-pressure-gradient supersonic boundary-layer flows have been very limited so far. Recent studies include the 'extended temporal' simulation of Maeder, Adams & Kleiser (2001), the quasi-periodic simulation of Guarini *et al.* (2000), and the fully spatial DNS of Pirozzoli, Grasso & Gatski (2004). These studies have further confirmed that a modified form of the wall law holds for the Van Driest-transformed mean velocity profile, and that the distribution of the density-scaled Reynolds stresses closely follows the universal distribution found in the incompressible case.

With regard to the dynamics of coherent structures of supersonic boundary layers, experimental results are scarce, mainly because of difficulties in resolving the very small vortices found at the high Reynolds numbers typical of supersonic experimental arrangements, and knowledge is mainly limited to the large-scale motions in the outer layer. Most of the available supersonic experimental data reviewed by Spina,

Smits & Robinson (1994) indicate little influence of compressibility on the large-scale turbulent boundary-layer motions and on the characteristic time scales, convection velocities and vortex angles. Robinson (1989) performed dual hot-wire measurements in a supersonic boundary layer at $M = 2.97$, $Re_\theta = 15\,000$, and analysed one- and two-point correlations to characterize coherent motions. The author concluded that large-scale structures are present throughout the boundary layer, whose slope with respect to the wall ranges from 5° at $y^+ = 29$ to 30° at $y/\delta = 0.6$. Spina & Smits (1987) and Spina, Donovan & Smits (1991) analysed the two-point space–time correlations in the outer part ($y^+ > 650$) of a canonical supersonic boundary layer at $M = 2.9$, $Re_\theta = 81\,000$. Those studies confirmed the existence of outer-layer structures similar to the turbulent bulges observed in the incompressible boundary layer, whose size is of $O(\delta)$, and whose inclination with respect to the wall varies from 45° to 60°. Furthermore, their convection velocity is nearly constant and equal to 90 % of the free-stream velocity.

The structural features of supersonic wall turbulence were investigated in the studies of Maeder *et al.* (2001) (at $M = 3, 4.5, 6$, $Re_\theta \approx 3000$) and Pirozzoli *et al.* (2004) (at $M = 2.25$, $Re_\theta = 4263$). In particular, the latter paper revealed the occurrence of organized motions in the outer layer (turbulent bulges) separated from the surrounding essentially irrotational fluid by sharp interfaces having a three-dimensional character, and of elongated streaky structures of alternating high- and low-speed fluid in the very near-wall region. Martin (2004) observed a consistent decrease of both the streamwise extent and the spanwise spacing of streaks (in terms of wall units) for $M > 3$. Ringuette, Wu & Martin (2008) have performed a DNS of a supersonic boundary layer (at $M = 3$, $Re_\theta \approx 2500$), and found the same type of coherent structures as in subsonic and supersonic experiments, i.e. elongated streaks in the log region, and hairpin vortex packets, frequently located above low-momentum streaks. No quantitative information related to the geometric properties (size and orientation) of vortical structures in supersonic boundary layers is presently available in the literature.

The main objective of the present study is to quantitatively characterize the statistical features (orientation, size and circulation) of coherent vortical structures of compressible wall-bounded flows by means of a highly resolved direct numerical simulation of a supersonic turbulent boundary layer at $M = 2$, $Re_\theta = 949$ (based on the inlet conditions). In addition, we also aim at formulating a model for the most representative (in a statistical sense) outer-layer structures. The paper is organized as follows. The numerical methodology is described in § 2; in § 3, the techniques developed for educing the coherent structures are illustrated; the main results of the study are presented in § 4, which includes a quantitative statistical analysis of the geometrical features of boundary-layer vortices in terms of population, orientation, size and topological properties of the educed structures. Concluding remarks are given in § 5.

2. Computational strategy

In the present work we solve the full three-dimensional unsteady Navier–Stokes equations for a perfect gas cast in conservation form

$$\frac{\partial \boldsymbol{U}}{\partial t} + \sum_{j=1}^{3} \frac{\partial \boldsymbol{F}_j}{\partial x_j} = \sum_{j=1}^{3} \frac{\partial \boldsymbol{G}_j}{\partial x_j}, \tag{2.1}$$

where

$$\boldsymbol{U} = \left\{ \begin{array}{c} \rho \\ \rho u_i \\ \rho E \end{array} \right\} \quad (i = 1, 2, 3),$$

is the vector of the conservative variables and

$$\boldsymbol{F}_j = \left\{ \begin{array}{c} \rho u_j \\ \rho u_i u_j + p\delta_{ij} \\ \rho E u_j + p u_j \end{array} \right\}, \quad \boldsymbol{G}_j = \left\{ \begin{array}{c} 0 \\ \sigma_{ij} \\ \sigma_{ij} u_i + k \dfrac{\partial T}{\partial x_j} \end{array} \right\} \quad (i = 1, 2, 3),$$

are the Eulerian and viscous fluxes in the jth coordinate direction, respectively; ρ is the density, u_i is the velocity component in the ith coordinate direction, p is the thermodynamic pressure, and

$$\sigma_{ij} = 2\,\mu S_{ij} - \tfrac{2}{3}\,\mu\, S_{kk}\,\delta_{ij},$$

is the viscous stress tensor, and $S_{ij} = (u_{i,j} + u_{j,i})/2$. The molecular viscosity is assumed to obey Sutherland's law, and the thermal conductivity is related to μ through the relation $k = c_p\,\mu/Pr$ (the molecular Prandtl number is assumed to be 0.72).

The computational strategy to solve the governing equations relies on a finite-difference approach that has been extensively validated in previous works both for isotropic decaying compressible turbulence and for wall-bounded turbulent supersonic flows (Pirozzoli & Grasso 2004, 2006). In particular, the Eulerian fluxes are discretized by means of a linear seventh-order central upstream approximation with local Lax–Friedrichs flux splitting, the viscous fluxes are approximated using a fourth-order compact-difference scheme, and time integration is performed by means of a classical four-stage fourth-order explicit Runge–Kutta algorithm.

The selected computational domain has an overall size $L_x \times L_y \times L_z = 25\delta_0 \times 3\delta_0 \times 3.7\delta_0$ where x, y and z stand, respectively, for the streamwise, wall normal and spanwise directions, and δ_0 is the boundary-layer thickness at the inlet section ($x = 0$). The domain is discretized with a grid consisting of $1809 \times 180 \times 225$ points that are uniformly distributed in the streamwise and spanwise directions. The mesh is stretched in the wall-normal direction (with 30 points in the buffer region up to $y^+ = 30$) according to a hyperbolic sine mapping function up to the boundary-layer edge, and according to a geometric progression up to the upper boundary of the computational box. In terms of wall units, the streamwise and spanwise mesh spacings are $\Delta x^+ = \Delta z^+ = 4.5$; the spacing in the wall normal direction varies from $\Delta y^+ = 0.95$ (at the wall) to $\Delta y^+ = 4.1$ (at the boundary-layer edge). Wall units are defined in terms of the friction velocity and of the viscous length scale evaluated at the wall ($u_\tau = \sqrt{\tau_w/\rho_w}$, $\delta_v = \nu_w/u_\tau$). Scaling with 'local' viscous units, while being dimensionally sound, does not lead to a compressible analogue of the wall law (Smits & Dussauge 2006).

The enforcement of initial and inlet boundary conditions is based on the approach developed by Sandham, Yao & Lawal (2003), and subsequently extended by Li & Coleman (2003) to supersonic flows. The basic idea is to consider a mean turbulent boundary-layer profile with superposed fluctuations that mimic the organized motions of the inner and outer part of the boundary layer (lifted streaks and large eddies, respectively). The approach has been extensively tested in the literature, and shown to yield faster transition to a fully developed turbulent state compared to conventional approaches (e.g. forcing through blowing and suction, recycling techniques, etc.).

x/δ_0	M_e	Re_δ	Re_θ	Re_τ	C_f	$H(\delta^*/\theta)$	T_w/T_e	μ_w/μ_e
0	2.0	13500	949	278	3.54×10^{-3}	3.19	1.717	1.568
15	2.0	14500	1180	270	3.22×10^{-3}	3.61	1.717	1.568
25	2.0	17400	1350	358	3.05×10^{-3}	3.62	1.717	1.568

TABLE 1. Boundary-layer properties at several streamwise stations (inlet section, beginning and end of fully developed turbulence). Subscripts: e indicates properties outside the boundary layer, w indicates wall properties. $Re_\delta=\rho_e u_e\delta/\mu_e$, $Re_\theta=\rho_e u_e\theta/\mu_e$, $Re_\tau=\rho_w u_\tau\delta/\mu_w=1/\delta_v$.

The mean Van Driest transformed velocity distribution has been prescribed according to (Guarini *et al.* 2000)

$$\overline{u}^+_{vd}=\begin{cases}\dfrac{1}{\kappa}\log(1+\kappa y^+)+C_1\left(1-\mathrm{e}^{-y^+/\eta_1}-\dfrac{y^+}{\eta_1}\mathrm{e}^{-by^+}\right)\\ \quad+\dfrac{1}{\kappa}\left[\left(\dfrac{y}{\delta}\right)^2-\left(\dfrac{y}{\delta}\right)^3+6\Pi\left(\dfrac{y}{\delta}\right)^2-4\Pi\left(\dfrac{y}{\delta}\right)^3\right] & (y<\delta),\\ u_{\infty vd}/u_\tau & (y\geqslant\delta),\end{cases}\tag{2.2}$$

where $\overline{u}_{vd}$ incorporates the effect of variable density in the boundary layer (Smits & Dussauge 2006)

$$\overline{u}_{vd}=\int_0^{\overline{u}}\left(\frac{\overline{\rho}}{\overline{\rho}_w}\right)^{1/2}\mathrm{d}\overline{u},\tag{2.3}$$

and $\kappa=0.41$, $C=5.1$, $\Pi=0.20$, $C_1=C-\log\kappa/\kappa$, $\eta_1=11$, $b=0.33$. Pressure has been assumed to be initially uniform, and the temperature distribution has been initialized using the Crocco–Busemann integral (White 1974). The characteristic parameters of the inlet boundary layer ($x/\delta_0=0$) are reported in table 1, where we also report the values computed from DNS at two downstream locations ($x/\delta_0=15$ and 25).

The velocity disturbances at the inlet are determined according to (Li & Coleman 2003)

$$\left.\begin{aligned}u'(x,y,z,t)&=\sqrt{\rho_w/\overline{\rho}(y)}\,u_\infty\sum_{j=1}^{5}a_j\,U_j(y)\,\sin\left[\omega_j\left(x/u_{c_j}-t\right)\right]\cos(2\pi z/\lambda_{z\,j}+\phi_j),\\ v'(x,y,z,t)&=\sqrt{\rho_w/\overline{\rho}(y)}\,u_\infty\sum_{j=1}^{5}b_j\,V_j(y)\,\sin\left[\omega_j\left(x/u_{c_j}-t\right)\right]\cos(2\pi z/\lambda_{z\,j}+\phi_j),\end{aligned}\right\}\tag{2.4}$$

where

$$U_j(y)=(y/\hat{y}_j)\,\mathrm{e}^{-y/\hat{y}_j},\qquad V_j(y)=(y/\hat{y}_j)^2\,\mathrm{e}^{-(y/\hat{y}_j)^2}.$$

The inner-layer disturbances ($j=1$) correspond to streaks and associated streamwise vortices propagating at a speed $10\,u_\tau$ with maximum amplitude at $y^+=12$, spanwise spacing $\lambda_z^+\approx128$ and streamwise wavelength $\lambda_x^+\approx500$. The outer-layer disturbances ($j=2,\ldots,5$) represent large vortical structures that scale in outer units and propagate with a convection velocity $0.75\,u_\infty$. The amplitudes of the various modes (a_j, b_j, see table 2) have been selected so as to closely reproduce the distribution of the Reynolds stress found in canonical fully developed boundary layers. In order to break any remaining symmetries due to the deterministic specification of inlet disturbances, divergence-free random velocity fluctuations with a maximum amplitude

j	$\hat{y}_j$	a_j	b_j	ω_j	u_{cj}	λ_{zj}	ϕ_j
1	$12.0\delta_v$	1.33	−0.25	$0.108u_\tau/\delta_v$	$10u_\tau$	$128\delta_v$	0.0
2	$0.298\delta_0$	0.33	−0.07	$0.839u_\infty/\delta_0$	$0.75u_\infty$	$L_z/2$	0.1
3	$0.447\delta_0$	0.33	−0.07	$0.419u_\infty/\delta_0$	$0.75u_\infty$	$L_z/4$	0.2
4	$0.596\delta_0$	0.33	−0.07	$0.210u_\infty/\delta_0$	$0.75u_\infty$	$L_z/6$	0.3
5	$0.447\delta_0$	0.33	−0.07	$0.336u_\infty/\delta_0$	$0.75u_\infty$	L_z	0.4

TABLE 2. Parameters for synthetic inlet forcing of DNS (as from equation (2.4)).

$u'_{rms}/u_\infty = 4\,\%$ have been added within the boundary layer (Li & Coleman 2003). Finally, the spanwise velocity component is determined assuming that the synthetic velocity field is solenoidal.

Zero wall-normal gradient has been enforced for temperature and pressure, and homogeneous Dirichlet boundary conditions for all velocity components have been specified at the no-slip adiabatic wall. A buffer layer is used to drive the flow to a uniform state towards the outlet boundary, where variables are extrapolated from the interior. Non-reflecting boundary conditions are specified at the upper boundary so as to minimize spurious reflections of disturbances back into the computational domain, and periodic boundary conditions are used in the spanwise direction to exploit homogeneity. The numerical algorithm and the adequacy of the computational mesh have been extensively tested in preliminary grid-sensitivity studies. In particular, the selected spanwise size of the domain is sufficient to accommodate approximately eight streaks ($L_z^+ \approx 1024$), and it guarantees that the two-point correlations of all flow variables drop to zero sufficiently fast so as not to inhibit the turbulence dynamics.

At the selected flow conditions, a fully developed turbulent state is observed starting from $x/\delta = 15$, where both the skin friction and the shape factor attain values in agreement with those reported by Smits & Dussauge (2006). The turbulent Mach number is found to be small throughout the domain ($M_t = \sqrt{\widetilde{u''^2}}/\bar{a} \leqslant 0.27$), thus preventing the manifestation of genuine compressibility effects, such as the occurrence of eddy shocklets (Pirozzoli & Grasso 2004).

3. Eduction of vortical structures

A fundamental issue in the analysis of coherent vortical structures is the definition of what a vortex is meant to be. According to Robinson *et al.* (1989), 'a vortex exists when instantaneous streamlines mapped onto a plane normal to the vortex core exhibit a roughly circular or spiral pattern, when viewed from a reference moving with the centre of the vortex core'. In practice, the identification of a vortex is still an issue (for a review of the subject, see Chakraborty, Balachandar & Adrian 2005). In the present work, we have followed the topological definition originally proposed by Chong, Perry & Cantwell (1990), and later applied to compressible isotropic turbulence by Pirozzoli & Grasso (2004).

Let $\boldsymbol{A}$ be the velocity gradient tensor ($\boldsymbol{A} = \nabla \boldsymbol{u}$), $\boldsymbol{A}^*$ be its traceless part ($\boldsymbol{A}^* = \boldsymbol{A} - \frac{1}{3}\nabla \cdot \boldsymbol{u}\, \boldsymbol{I}$), and Q^* ($= -\frac{1}{2} A^*_{ij} A^*_{ji}$) and R^* ($= -\frac{1}{3} A^*_{ij} A^*_{jk} A^*_{ki}$) be the second and third invariants (the first being identically zero) of $\boldsymbol{A}^*$. A vortex is identified as a connected region where $\boldsymbol{A}^*$ has one real eigenvalue (λ_r) and two complex conjugate ones ($\lambda_c^\pm = \lambda_{cr} \pm \mathrm{i}\,\lambda_{ci}$), which amounts to requiring that the discriminant of the characteristic

equation of $\boldsymbol{A}^*$

$$\Delta = Q^{*3} + \tfrac{27}{4} R^{*2}, \tag{3.1}$$

is positive. As pointed out by Zhou *et al.* (1999), the local motion at the locations where $\Delta > 0$ (corresponding to core centres) is made up of the superposition of a straining motion of strength λ_r in the associated eigendirection ($\boldsymbol{v}_r$), and a spiralling motion with angular velocity λ_{ci} in the plane defined by the vectors $\boldsymbol{v}_{cr}$, $\boldsymbol{v}_{ci}$ (where $\boldsymbol{v}_c^{\pm} = \boldsymbol{v}_{cr} \pm \mathrm{i}\, \boldsymbol{v}_{ci}$ are the eigendirections associated with $\lambda_c^{\pm}$). In the present study coherent vortical structures are identified as those regions where the 'swirling strength' exceeds a suitable threshold ($\lambda_{ci}^2 \geqslant \epsilon^2$; the selected value of the threshold is specified in the discussion of the results).

Once the vortical structures are educed, properties such as orientation and size are quantitatively determined. With regard to vortex core orientation, we have considered four different criteria, based on: (i) local vorticity direction ($\boldsymbol{\omega}$-criterion); (ii) swirl plane normal direction ($\boldsymbol{v}_{ax}$-criterion, $\boldsymbol{v}_{ax} = \boldsymbol{v}_{cr} \times \boldsymbol{v}_{ci}$); (iii) local strain direction ($\boldsymbol{v}_r$-criterion); (iv) eigendirection associated with the minimum eigenvalue ($\boldsymbol{e}_1^H$) of the pressure Hessian (p-criterion).

It is a simple matter to show that in a purely rotational motion (i.e. if $\boldsymbol{A}^*$ is antisymmetric), the first three criteria are equivalent. The p-criterion relies on the assumption that vortex structures are tubular, and therefore pressure must attain a minimum in a plane normal to the vortex axis, to which are associated the two largest positive eigenvalues of the pressure Hessian. The eigendirection corresponding to the remaining eigenvalue ($\boldsymbol{e}_1^H$, which is the smallest in modulus, and which can be either positive or negative) is therefore expected to be associated with the direction parallel to the vortex axis. We observe that both the $\boldsymbol{v}_r$-criterion and the p-criterion do not yield a unique local vortex orientation, being defined in terms of eigendirections. To remove such ambiguity we select for the local vortex orientation the direction closer to the local vorticity direction out of the possible two.

Preliminary assessment of the various criteria has shown potential failure in the presence of intense mean shear. For example, for unidirectional uniform shear the $\boldsymbol{\omega}$- and $\boldsymbol{v}_{ax}$ criteria favour directions normal to the shear plane, the $\boldsymbol{v}_r$-criterion favours directions aligned with the shear direction, while the direction predicted by the p-criterion lies in between. In order to alleviate such deficiency, the geometrical properties of vortical structures are determined by subtracting out the mean shear, as was also done by Robinson (1991*b*). We point out that, in principle, mean shear and turbulent fluctuations cannot be decoupled. However, as will be shown in the following, most of the educed structures are detached from the wall in the sense of Townsend. According to the analysis of Del Álamo *et al.* (2006), detached eddies play little part in the establishment of the mean shearing field, and consequently it is reasonable to decouple them from the mean field.

Typical visualizations of vortex cores in the outer region of the boundary layer are represented in figure 1, where we report vector fields with modulus λ_{ci}^2 and direction corresponding to the various vortex orientation criteria. The figure indicates good alignment of the vector fields with the local direction of the vortex tubes (constructed as iso-surfaces of the swirling strength). While all criteria are nearly equivalent for vortices placed sufficiently for away from the wall, some differences are observed for vortices located very close to the wall.

A more detailed analysis has shown uncertainties when using the p-criterion. In particular, such a criterion correctly identifies cores of strong vortices, whereas for weak vortices and for points near the boundary of strong ones it exhibits a tendency

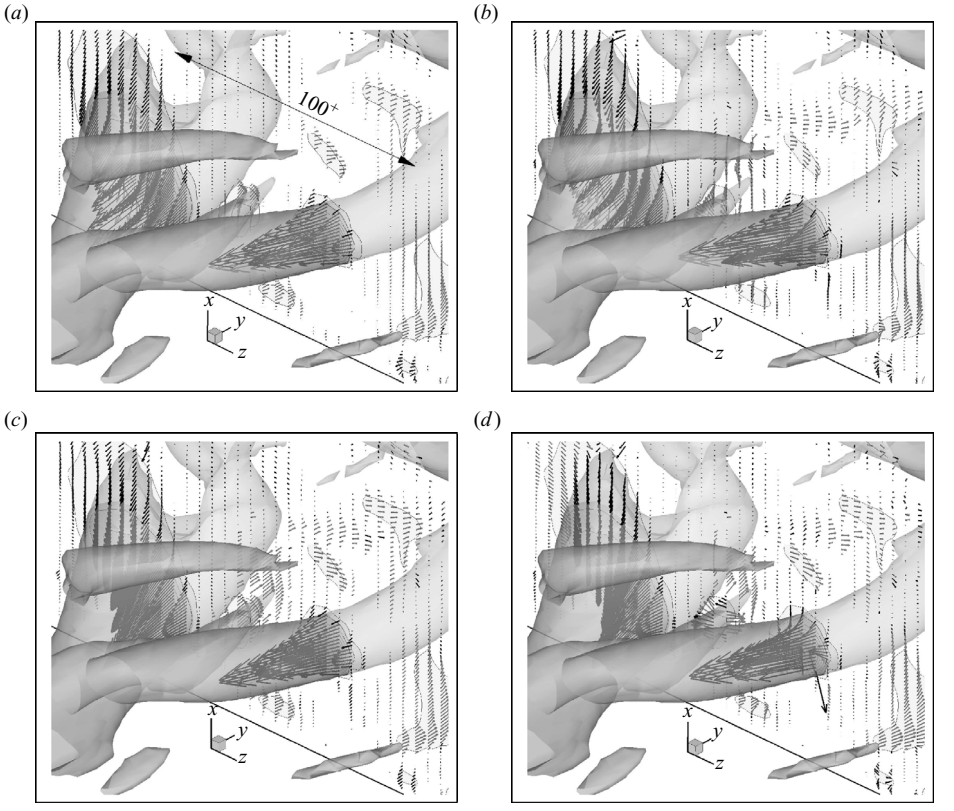

FIGURE 1. Visualization of vortex cores in the boundary layer. Tubes represent isosurfaces of $\lambda_{ci}^2 = 5\,u_\infty^2/\delta_0^2$ and vectors indicate (*a*) $\lambda_{ci}^2\hat{\boldsymbol{\omega}}$; (*b*) $\lambda_{ci}^2\hat{\mathbf{v}}_{ax}$; (*c*) $\lambda_{ci}^2\hat{\mathbf{v}}_r$; (*d*) $\lambda_{ci}^2\hat{\mathbf{e}}_1^H$.

to yield core direction in the plane of the core, rather than normal to it. For this reason the *p*-criterion has not been considered in the quantitative analysis of vortex orientations.

We point out that in the analysis that follows, all the statistical properties related to vortex orientation and size are weighted by the swirling strength λ_{ci}^2, in order to give more importance to regions of intense vortical motion.

4. Results

In order to highlight the qualitative features of the flow field, in figure 2 we report the contours of the streamwise velocity fluctuations in a plane parallel to the wall (at $y^+ = 15$), with superposed vortical structures visualized by means of the swirling strength criterion. Many of the features reported by Robinson (1991*a*) for incompressible boundary layers are also found in the present DNS study. The velocity field in the viscous sublayer and in the buffer region is organized into alternating elongated narrow streaks of high-speed and low-speed fluid (represented, respectively, as light and grey shades), with a characteristic length of $O(1000)$ wall units (such a value being inferred from inspection of many data sets), which compares well with low-speed boundary-layer data (Kline *et al.* 1967). Strong vortices (both quasi-streamwise vortices and hairpins) are mainly associated with the low-speed streaks, and have a characteristic length of $O(100)$ wall units. The close relation between low-speed streaks

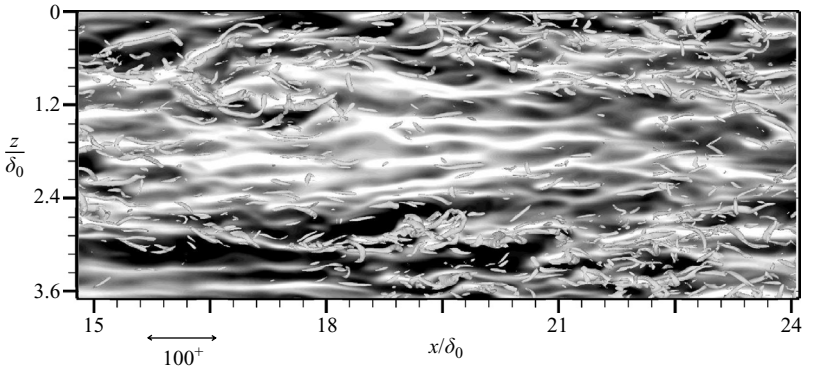

FIGURE 2. Contours of u''/u_∞ in the buffer zone ($y^+ = 15$), with superposed iso-surfaces of swirling strength ($\lambda_{ci}^2 = 5\,u_\infty^2/\delta_0^2$). Contour levels from -0.2 to 0.2; light shades indicate $u'' > 0$, grey shades indicate $u'' < 0$.

and coherent vortices has already been observed by several authors (Jiménez & Pinelli 1999; Ringuette *et al.* 2008), and can be equally well explained in the light of the theories for near-wall turbulence self-sustainment proposed by Hamilton *et al.* (1995) and Chernyshenko & Baig (2005).

In figure 3, we report a three-dimensional view of the vortex cores detected with the iso-surface of the swirling strength corresponding to $\lambda_{ci}^2 = 5\,u_\infty^2/\delta_0^2$. In the figure, near-wall structures are rendered in light shades, whereas structures located away from the wall are depicted in dark shades. Figure 3 shows that the innermost layer is populated by quasi-streamwise vortices inclined at a small angle with respect to the (x, z)-plane; far from the wall, most of the observed structures have a cane-like shape, as also observed by Robinson (1991*b*). Visual analysis of many flow samples shows the occurrence of: (i) hairpin-shaped vortices, occasionally arranged in packets (see figure 3*a*), as observed by Adrian *et al.* (2000) and Ringuette *et al.* (2008); (ii) vortex arches (see figure 3*b*); and (iii) few inverted arches (figure 3*c*). As also found by previous investigators, hairpin vortices with a well-defined distinction between counter-rotating legs and a spanwise head are rather rare.

4.1. *Mean and statistical flow properties*

The statistical properties of the boundary layer have been obtained by assuming homogeneity in the spanwise direction, and taking time-averages of the computed solution once the flow is statistically steady. For this purpose, 100 flow samples (equally spaced in time) have been collected over approximately 10 non-dimensional time units (δ_0/u_∞), which is found to be long enough to obtain accurate estimates of up to second-order statistics. In the analysis that follows, the instantaneous flow-field variables are decomposed using either a Reynolds decomposition $f = \overline{f} + f'$, or a density-weighted (Favre) decomposition $f = \tilde{f} + f''$, where $\tilde{f} = \overline{\rho f}/\overline{\rho}$.

For the purpose of validating the present simulation we compare the computed mean velocity, Reynolds stress and root-mean-square (r.m.s.) vorticity components with the DNS of incompressible channel flow (at $Re_\tau = 550$) of del Álamo & Jiménez (2003). The distribution of the Van Driest-transformed mean streamwise velocity is shown in a semi-logarithmic plot in figure 4. In the figure we also report the expected linear scaling in the viscous sublayer (strictly valid if the density is constant, as approximately verified in the near-wall region of adiabatic plates, see § 7.2 of

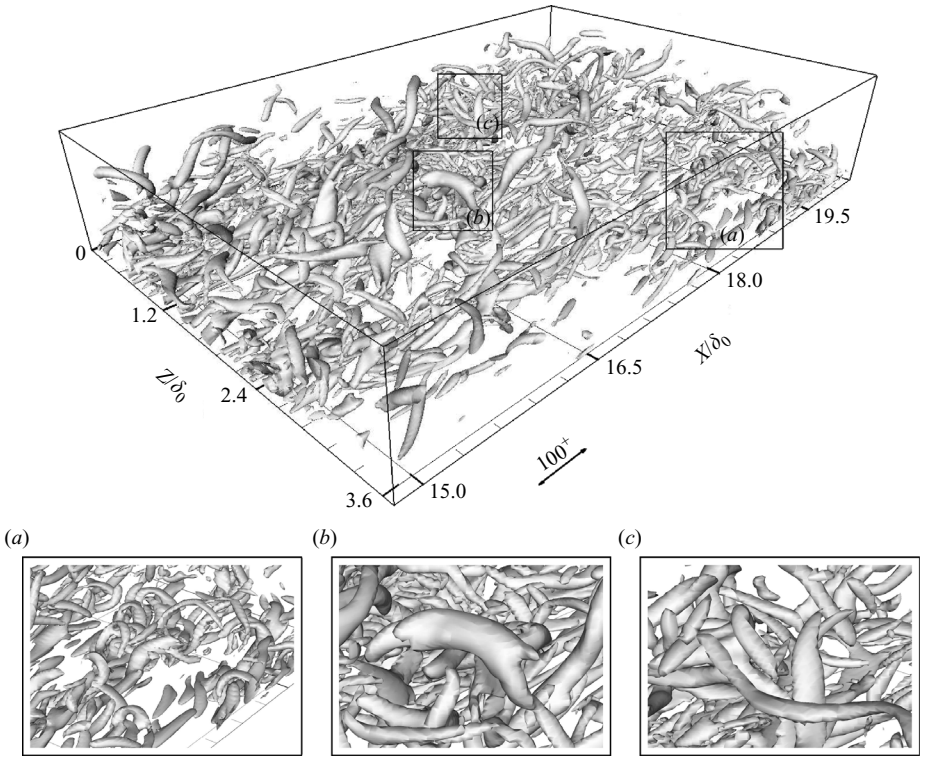

FIGURE 3. Perspective view of coherent structures in the boundary layer ($\lambda_{ci}^2 = 5\,u_\infty^2/\delta_0^2$). ($a$–$c$) Enlargements of corresponding parts in the main figure.

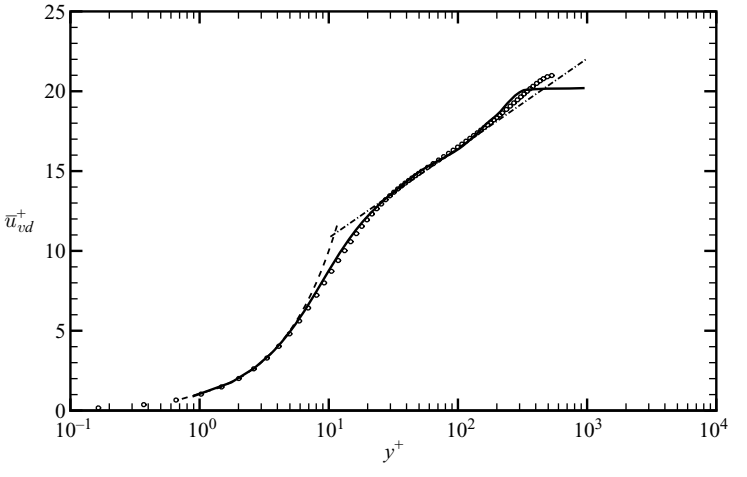

FIGURE 4. Distribution of Van Driest transformed mean streamwise velocity (equation (2.3)) at $x/\delta_0 = 25$ in inner scaling: ——, DNS; – – –, equation (4.1); - · -, equation (4.2); ○, DNS of channel flow at $Re_\tau = 550$ (del Álamo & Jiménez 2003).

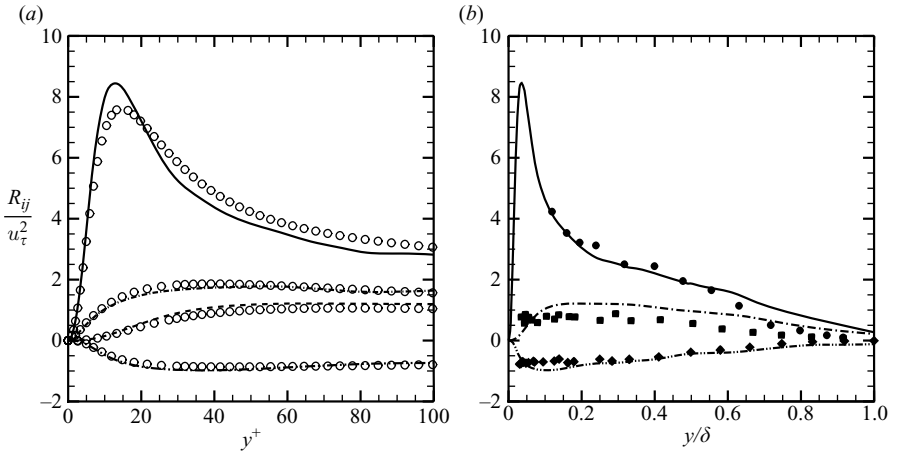

FIGURE 5. Distribution of density-scaled Reynolds stress components $R_{ij} = (\overline{\rho}/\overline{\rho}_w)\,\widetilde{u_i'' u_j''}$ at $x/\delta_0 = 25$ in (*a*) inner scaling and (*b*) outer scaling. ——, R_{11}; – – –, R_{22}; - · -, R_{33}; - · · -, R_{12}. Open symbols: DNS of channel flow at $Re_\tau = 550$ (del Álamo & Jiménez 2003). Filled symbols: experimental data at $M = 2.32$, $Re_\theta = 4700$ (Eléna & Lacharme 1988).

Smits & Dussauge 2006)

$$\overline{u}_{vd}^+ = y^+, \tag{4.1}$$

and the logarithmic scaling in the overlap region

$$\overline{u}_{vd}^+ = C + \frac{1}{k}\log y^+, \tag{4.2}$$

where the von Kármán constant is set to $k = 0.41$, and the log law constant is set to $C = 5.2$, as found in previous supersonic DNS (Pirozzoli *et al.* 2004) and in experiments (Eléna & Lacharme 1988 report $C = 5.17$). The results are in excellent agreement with the incompressible DNS data, except for some differences in the outermost region, where the selected Re_τ is different from del Álamo & Jiménez (2003). The figure also shows that the viscous sublayer law holds up to $y^+ \approx 7$, and the log region extends approximately from $y^+ = 40$ to $y^+ = 140$. Consistent with experimental and theoretically predicted results at very low Reynolds number (Smits & Dussauge 2006), we observe a relatively small wake (the estimated wake law constant $\Pi \approx 0.175$). In the following discussion we will often refer to the region below $y^+ = 40$ (that includes the viscous sublayer and the buffer layer) as the 'inner layer', and similarly we will refer to the region above $y^+ = 40$ (that includes the logarithmic layer and the wake region) as the 'outer layer'. The distributions of the density-scaled Reynolds-stress components are reported in figure 5. In agreement with Morkovin's hypothesis (Morkovin 1961), the scaled DNS data agree well with the incompressible channel-flow data of del Álamo & Jiménez (2003), the main difference being a larger amplitude of the peak streamwise turbulence intensity, consistent with the findings of Gatski & Erlebacher (2002) and Pirozzoli *et al.* (2004). To further assess the global behaviour of the external layer, figure 5(*b*) compares the distributions of the Reynolds stresses to the supersonic boundary-layer measurements of Eléna & Lacharme (1988), and confirms the quality of the present simulation.

Figure 6 shows the distribution of the computed r.m.s. vorticity components in wall units. In agreement with the findings of Klewicki (1997), the spanwise vorticity fluctuations (ω_z') are significantly larger than either the streamwise (ω_x') or the wall-normal

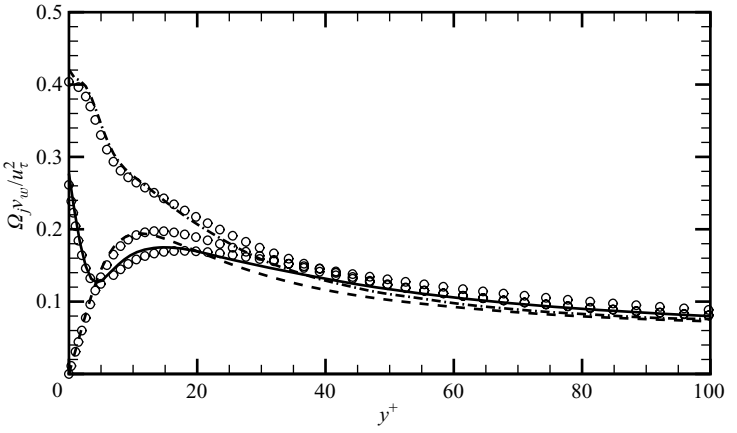

FIGURE 6. Distribution of r.m.s. vorticity components $\Omega_i = (\overline{\omega_i'^2})^{1/2}$ at $x/\delta_0 = 25$ in wall units: ——, streamwise component; – – –, wall-normal component; - · -, spanwise component. Symbols: DNS of channel flow at $Re_\tau = 550$ (del Álamo & Jiménez 2003).

(ω_y') fluctuations for $y^+ < 25$; for $y^+ > 30$, the vorticity fluctuations become nearly isotropic (being $\omega_x' \approx \omega_y' \approx \omega_z'$). Consistent with the data of del Álamo & Jiménez (2003), ω_x' attains a peak at $y^+ \approx 16$, and ω_y' is maximum at $y^+ \approx 12$.

4.2. *Vortex orientation statistics*

The issues related to the orientation of vortical structures in wall turbulence have been widely studied in the literature. An often quoted result is that vortical structures are mainly inclined at 45° with respect to the wall. Theodorsen (1952) first postulated the existence of horseshoe-shaped vortices inclined along the principal extensive strain direction (making an angle of 45° with respect to the wall), and his conclusions were confirmed by the flow visualization of individual hairpin vortices of Head & Bandyopadhyay (1981). Ong & Wallace (1998) arrived at similar conclusions from the analysis of the joint p.d.f. of the vorticity components in the longitudinal wall-normal (x, y)-plane. Ganapathisubramani *et al.* (2006) focused their attention on the necks of hairpin structures, and found that their most probable elevation angle is again approximately 45°.

In the present work we define the local orientation of vortical structures in terms of two angles: the elevation angle (θ_e), i.e. the angle formed with the wall plane, and the projection angle (θ_{zx}) in the wall plane. By convention, the projection angle is measured with respect to the positive z-direction, and counted moving in the positive x-direction (see figure 16). For example, the projection angle associated with the mean vorticity vector (which points in the negative z-direction) is $\theta_{zx} = \pm 180°$.

The statistical orientation of the educed coherent structures is completely characterized by introducing the joint p.d.f. (P) of the elevation and projection angles. We point out that, in the case of an isotropic random vector field, we would have $P(\theta_{zx}, \theta_e) \sim \cos\theta_e$. Hence, to avoid biasing towards small values of θ_e, we introduce a scaled p.d.f., defined as

$$\tilde{P}(\theta_{zx}, \theta_e) = \frac{P(\theta_{zx}, \theta_e)/\cos\theta_e}{\displaystyle\int_{-\pi/2}^{\pi/2}\int_{-\pi}^{\pi} P(\theta_{zx}, \theta_e)/\cos\theta_e \,\mathrm{d}\theta_{zx}\mathrm{d}\theta_e}, \tag{4.3}$$

which yields $\tilde{P}(\theta_{zx}, \theta_e) \equiv 1/2\pi^2$ for an isotropic vector field.

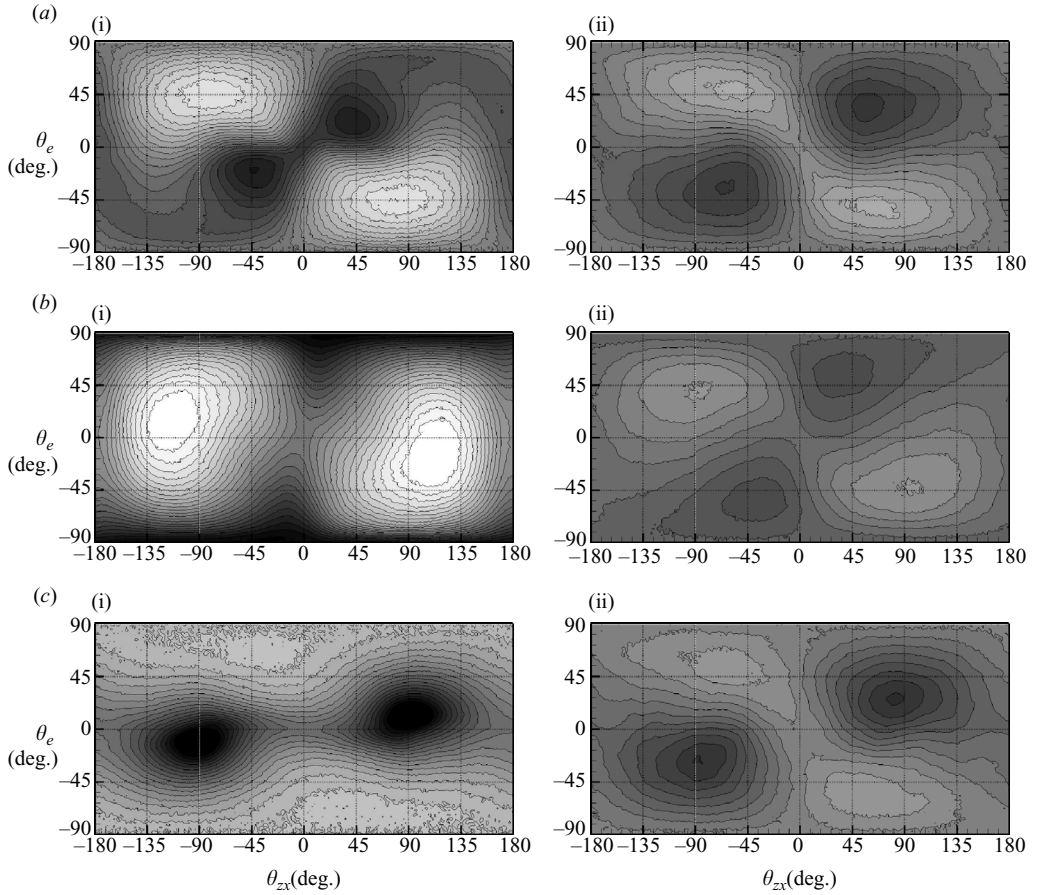

FIGURE 7. Scaled joint p.d.f. of vortex orientation ($\tilde{P}(\theta_{zx}, \theta_e)$) for various vortex orientation criteria. (*a*) $\hat{\boldsymbol{\omega}}$-criterion; (*b*) $\hat{\boldsymbol{v}}_{ax}$-criterion; (*c*) $\hat{\boldsymbol{v}}_r$-criterion. Twenty-four equally spaced contour levels from 10^{-6} to 10^{-4} (grey shades indicate larger values). (i) Viscous + buffer layer ($y^+ \leqslant 40$). (ii) Log-layer + wake ($y^+ \geqslant 40$).

Figure 7 reports the distribution of $\tilde{P}(\theta_{zx}, \theta_e)$ separately for both the inner and the outer layer. The figure indicates overall agreement of all orientation criteria in the outer layer, whereas strong sensitivity to the eduction criterion are found in the inner layer. The discrepancies are most probably due to the observed biasing of the various vortex orientation criteria in the presence of intense strain.

In the commonly accepted scenario, the near-wall boundary layer is populated by quasi-streamwise vortices with small inclination with respect to the wall plane. Figure 7 shows that the only criterion which is consistent with such a scenario is the one based on the local strain direction ($\boldsymbol{v}_r$-criterion), which indeed suggests the presence of quasi-streamwise vortex cores inclined at $\theta_e \approx \pm 10^\circ$.

In the outer layer, the p.d.f. maps show a preference for vortex directions in the first and third quadrant, thus indicating the prevalence of forward-leaning structures, with (weak) local maxima in the range $40^\circ \leqslant |\theta_{zx}| \leqslant 90^\circ$ and $25^\circ \leqslant |\theta_e| \leqslant 60^\circ$, depending upon the chosen eduction criterion. No distinct peaks associated with quasi-streamwise vortices ($\theta_{zx} \approx \pm 90^\circ$, $\theta_e \approx 0^\circ$), clockwise ($\theta_{zx} \approx \pm 180^\circ$, $\theta_e \approx 0^\circ$) and counterclockwise heads ($\theta_{zx} \approx 0^\circ$, $\theta_e \approx 0^\circ$) are observed.

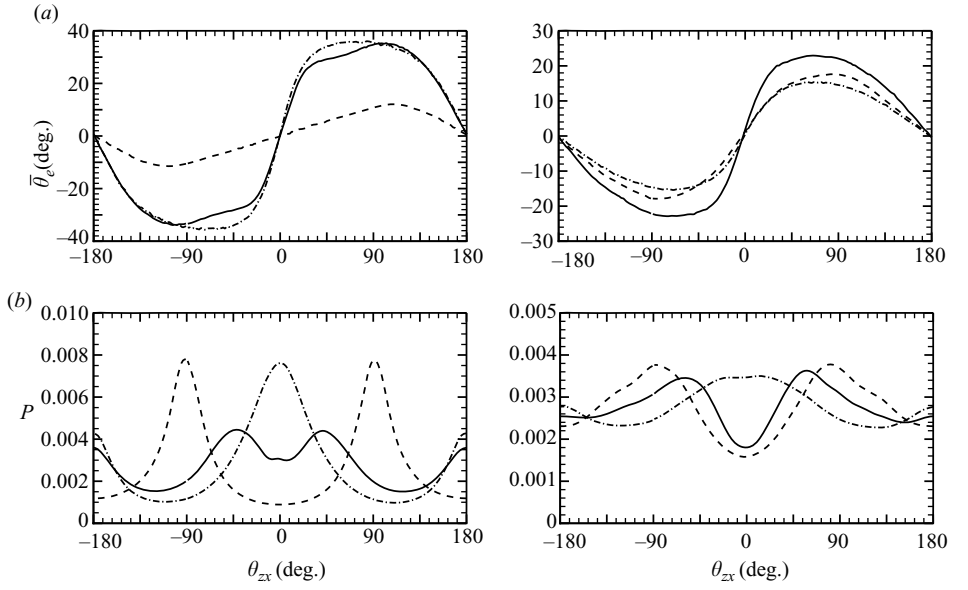

FIGURE 8. Distribution of (*a*) conditional expected value of θ_e and (*b*) probability density function of θ_{zx} for various vortex identification criteria in the inner layer (left-hand column) and in the outer layer (right-hand column). ——, $\boldsymbol{\omega}$-criterion; – – –, $\boldsymbol{v}_r$-criterion; - · -, $\boldsymbol{v}_{ax}$-criterion.

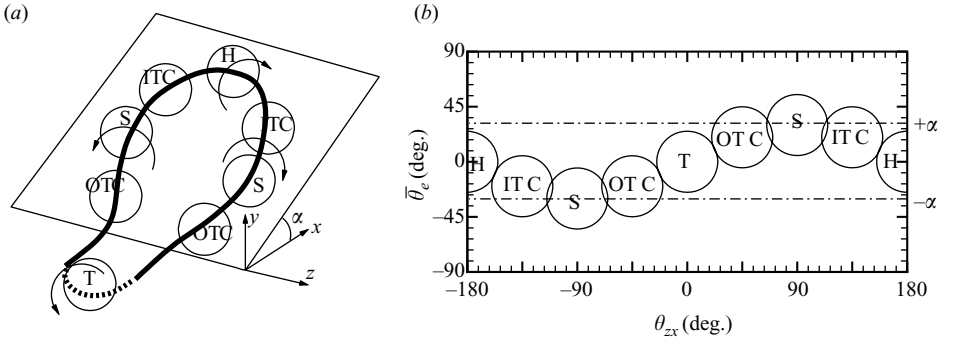

FIGURE 9. Sketch of representative vortex loop structure (*a*) and associated signature in the (θ_{zx}, θ_e)-plane (*b*). H, vortex head; ITC, inward-tilted vortex core; S, vortex sides; OTC, outward-tilted vortex core; T, vortex tail.

In figure 8 we report the distribution of the conditional expected value of the elevation angle as a function of the wall projection angle, defined as

$$\overline{\theta}_e(\theta_{zx}) = \int_{-\pi/2}^{\pi/2} \theta_e \, \tilde{P}(\theta_{zx}, \theta_e) \, \mathrm{d}\theta_e. \tag{4.4}$$

The figure shows a nearly sinusoidal dependence of $\overline{\theta}_e$ upon θ_{zx} in the outer layer, with peak values of $|\theta_e| = 15°$–$23°$, depending upon the selected vortex orientation criterion. We point out that a closed-loop structure, such as that sketched in figure 9, would yield a similar dependence. Specifically, if we assume for the loop a planar elliptical shape with an inclination α with respect to the forward direction, it is easy

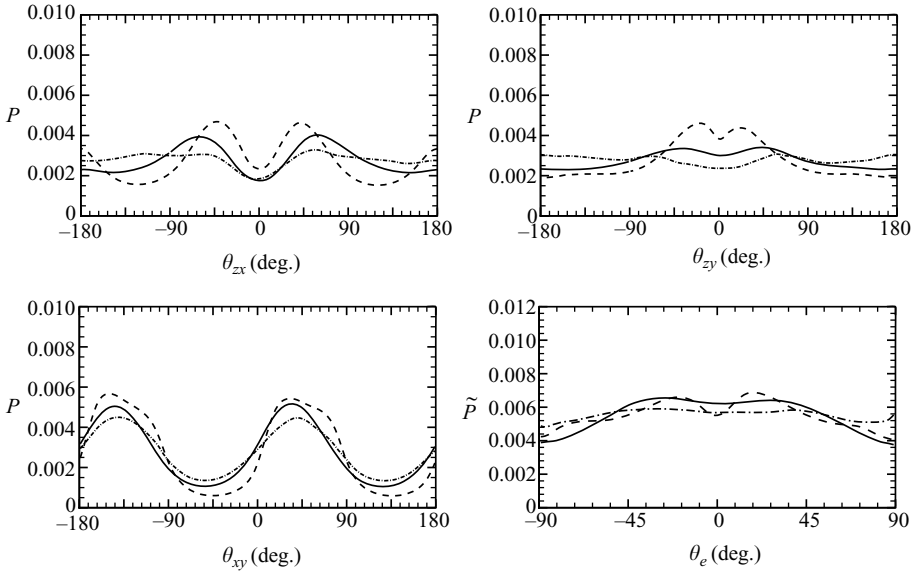

FIGURE 10. Probability density function of characteristic angles (ω-criterion). – – –, buffer layer; ——, log layer; - · -, wake region.

to verify that the following relationship between θ_{zx} and θ_e holds

$$\theta_e = \frac{\sin\alpha}{\sqrt{1+\cos^2\alpha\cot^2\theta_{zx}}}, \tag{4.5}$$

regardless of the aspect ratio of the loop. Equation (4.5) implies a quasi-sinusoidal dependence of θ_e upon θ_{zx}, with a variation from $-\alpha$ to $+\alpha$. This suggests that ring-like vortices leaning in the streamwise direction at an angle $\alpha = 15°$–$23°$ with respect to the positive streamwise direction can be regarded as the statistically representative outer-layer structures. Similar values of the inclination angle are also found from the analysis of the two-point streamwise momentum flux correlations (not reported), that yield an average orientation of the outer-layer structures of $\sim 18°$ (for $0.2 \leqslant y/\delta \leqslant 0.7$). This finding is consistent with the conditional eddy inclination angle reported by Hutchins *et al.* (2005) for low-speed boundary layers, but it differs from the values reported by Spina & Smits (1987) and Robinson (1989) for the average 'structure angles' in supersonic boundary layers.

It is important to observe that the inclination angle considered here represents in some sense a statistical average of the inclination of all vortical structures, including both quasi-streamwise vortices (which lie in wall-parallel planes) and hairpin vortices (which lie in planes inclined at 45° with respect to the wall). In this respect, we again recall that the DNS results (see figure 7) indicate that vortical structures are continuously distributed across a broad range of orientations. Therefore, discriminating between quasi-longitudinal vortices and hairpins is somewhat artificial. We will return to the issues related to the topology and inclination of the 'typical' structures in § 4.5.

To further characterize the statistical orientation of vortical structures, in figure 10 we report the univariate p.d.f. of the projection angles (in the three coordinate planes) and of the elevation angle. Figure 10 shows a statistical preference for $|\theta_{zx}| \approx 40°$ in

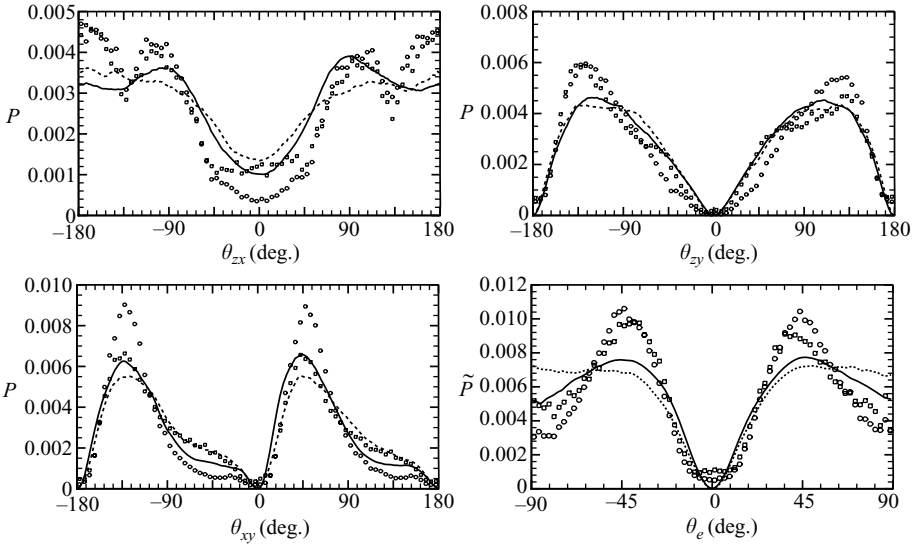

FIGURE 11. Probability density function of characteristic angles (vorticity criterion, mean shear included). ——, log layer; – – –, wake region. Symbols indicate experimental data (Ganapathisubramani *et al.* 2006); ○, $y^+ = 110$; □, $y/\delta = 0.53$.

the buffer zone and $|\theta_{zx}| \approx 60^\circ$ in the log layer, thus suggesting the prevalence of vortex cores tilted outwards (denoted by OTC in figure 9). Furthermore, the slight preference for $|\theta_{zx}| \approx 180^\circ$ with respect to $\theta_{zx} \approx 0^\circ$ suggests that heads (H, see figure 9) are statistically more frequent than tails (T, see figure 9). The distribution of $P(\theta_{xy})$ indicates a tendency for vortex cores to lean in the streamwise direction, with a peak projection angle of $\theta_{xy} \approx 33^\circ$ in the buffer region and $\theta_{xy} \approx 40^\circ$ in the outer layer, in agreement with the measurements of Ong & Wallace (1998). The distribution of $\tilde{P}(\theta_e)$ exhibits a peak at $\pm 18^\circ$ in the buffer region, whereas in the outer layer it shows a rather flat distribution in the range $|\theta_e| \leqslant 45^\circ$.

In order to compare our data with the experiment of Ganapathisubramani *et al.* (2006), we have also performed a statistical analysis restricted to the regions where the velocity gradient in planes parallel to the wall has a pair of complex conjugate eigenvalues, thus considering only the necks of hairpin vortices, and neglecting both spanwise and quasi-streamwise cores. The results reported in figure 11 exhibit the same trend as the experimental data, the main differences being the underestimation of the peak values of the p.d.f.'s, and are consistent with the flow visualizations of Head & Bandyopadhyay (1981), confirming that the most probable elevation angle of hairpin vortices is $\theta_e \approx 45^\circ$. The discrepancies with the experimental data are most probably due to a difference in the Reynolds number ($Re_\tau = 1160$ in the experiment), as well as to subtle differences in the eduction procedure.

As seen in the last two figures, the generally quoted angle of 45° is arrived at following different approaches, e.g. considering the statistics of the vorticity projection in the (x, y)-plane, or retaining (more or less arbitrarily) only the 'necks' of hairpins. However, it is our opinion that a convenient definition of the typical vortex inclination angle necessarily involves the analysis the statistical relation between the elevation and projection angles. Following this approach leads to a much smaller value of the expected inclination angle.

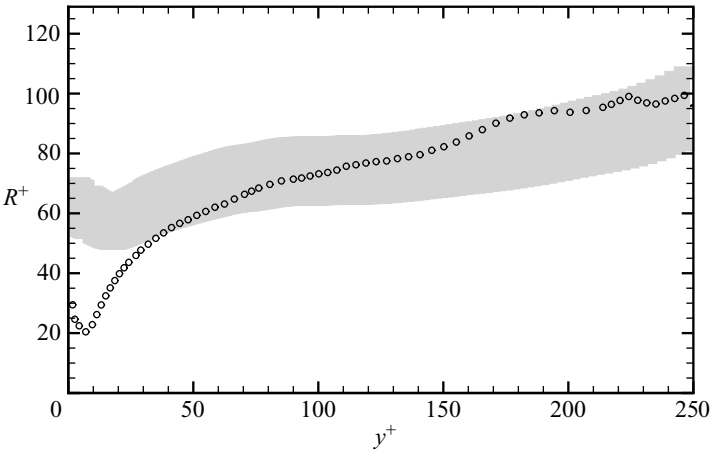

FIGURE 12. Distribution of mean radius of curvature of the vorticity field as a function of the wall distance in wall units. The shaded area marks the region where $27 < R/\eta < 35$.

4.3. *Vortex curvature statistics*

The geometrical features of vortical structures have been further characterized by considering the statistics of the curvature of vortex lines, defined as curves everywhere tangent to the local vorticity vector $\boldsymbol{\omega}$. The local radius of curvature of a vortex line can be defined as (Farin 1992)

$$R = \frac{\omega^3}{|\boldsymbol{\omega} \times (\nabla \boldsymbol{\omega} \cdot \boldsymbol{\omega})|}. \tag{4.6}$$

The distribution of the expected value of R (see figure 12) shows a consistent increase with the wall distance in the outer layer, with the mean radius varying between 60 and 100 wall units. Introducing the local dissipative length scale, defined as (Smits & Dussauge 2006)

$$\eta = \frac{1}{\sqrt{\overline{\rho}}} \left(\frac{\overline{\mu}^3}{\overline{\sigma'_{ij}\, u'_{i,j}}} \right)^{1/4},$$

the expected radius of curvature of the outer layer vortical structures scales as $27 < R/\eta < 35$, for $50 \leqslant y^+ \leqslant 200$.

4.4. *Vortex cores statistics*

In order to determine the characteristic size and circulation of the educed vortex structures we have analysed the flow field in the cross-stream (y, z)- and longitudinal wall-normal (x, y)-planes (also referred to as sampling planes). Candidate core centres in the sampling planes are then defined as points where: (i) the swirling strength attains a local maximum and is larger than a suitable threshold (ϵ); and (ii) the vorticity vector is nearly normal to the sampling plane. In addition, only those cores which induce a consistent swirling motion (either clockwise or counterclockwise) about their centre are retained for the statistical analysis (Carlier & Stanislas 2005).

Threshold independence and convergence of statistics is achieved assuming $\epsilon = 0.42\, u_\infty/\delta_0$, and retaining vortices whose axes make an angle with the normal to the sampling plane of less than 20°. The relative velocity field about the core centres is scanned in the sampling plane in the east, west, south and north directions, and four core radii (r_E, r_W, r_S, r_N) are identified where the tangential velocity attains

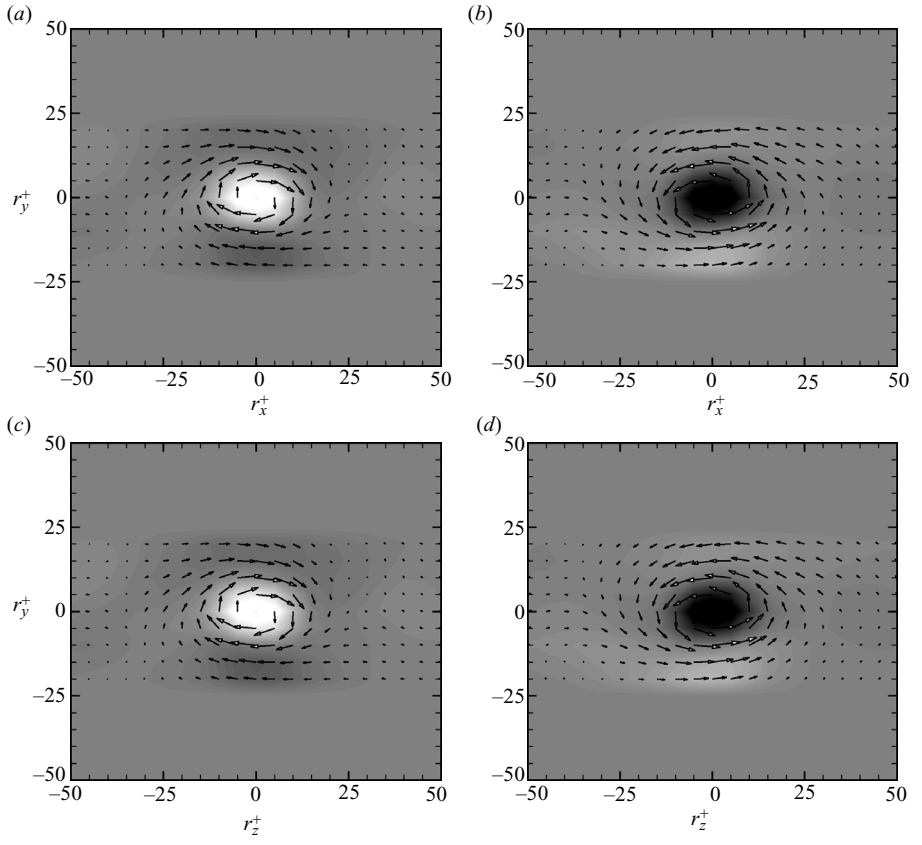

FIGURE 13. Average eddy structures in viscous + buffer layer : (*a*) (x, y)-plane, clockwise cores; (*b*) (x, y)-plane, counterclockwise cores; (*c*) (y, z)-plane, clockwise cores; (*d*) (y, z)-plane, counterclockwise cores. Vectors represent the induced velocity field, contours indicate average vorticity (contour levels from $-0.17\,u_\infty/\delta_0$ to $0.17\,u_\infty/\delta_0$).

its maximum values (v_E, v_W, v_S, v_N). The vortex core area is then estimated as $S = \pi(r_E + r_W)(r_S + r_N)/4$, and the core circulation, effective radius and effective induced velocity are determined according to

$$\Gamma_0 = \frac{\pi}{4}(r_E v_E + r_W v_W + r_S v_S + r_N v_N), \quad r_0 = \sqrt{\frac{S}{\pi}}, \quad v_0 = \frac{\Gamma_0}{2\pi r_0}.$$

The total vortex circulation (Γ_∞) is estimated from the core circulation, assuming that the velocity distribution is similar to the Lamb–Oseen vortex, which implies $\Gamma_\infty = \Gamma_0/(1 - 1/e)$.

Figures 13 and 14 show the average velocity vector plots (associated with both streamwise and cross-stream cores), respectively, in the inner and in the outer part of the boundary layer; in the figures we also report the contours of the computed out-of-plane vorticity component. Regardless of their nature (streamwise, spanwise, clockwise or counter-clockwise) all vortices exhibit the same qualitative flow pattern, with a spiralling motion about the vortex centre owing to the effect of vortex stretching in the direction normal to the plane under consideration. In the inner layer, vortex cores are nearly elliptical owing to the presence of intense shear, and they tend to become more circular in the outer layer.

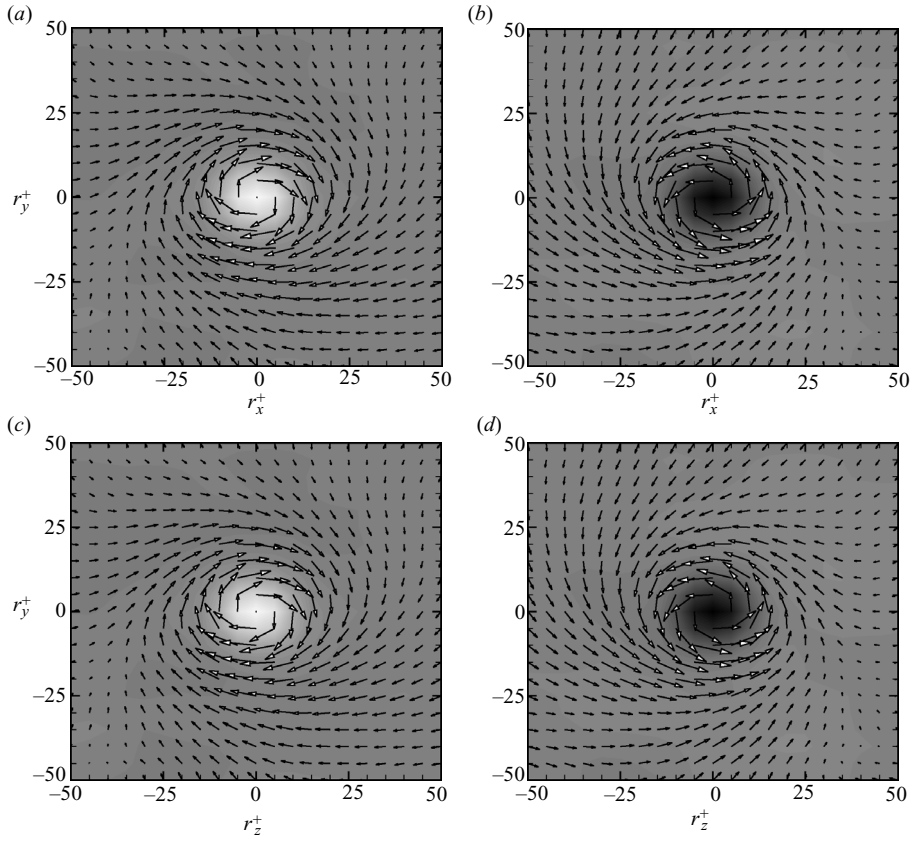

FIGURE 14. Average eddy structures in the log layer + wake region: (*a*) (x, y)-plane, clockwise cores; (*b*) (x, y)-plane, counterclockwise cores; (*c*) (y, z)-plane, clockwise cores; (*d*) (y, z)-plane, counterclockwise cores. Vectors represent the induced velocity field, contours indicate average vorticity (contour levels from $-0.17\,u_\infty/\delta_0$ to $0.17\,u_\infty/\delta_0$).

The computed distributions of the number density of vortex cores (that represents the number of detected vortex cores per unit surface in the sampling plane), their characteristic radius, their induced velocity, their total circulation, and their $x-$ and $y-$convection velocity components are reported in figure 15. The distributions of the number density of the quasi-streamwise and quasi-spanwise vortices (figure 15*a*) show a prevalence of streamwise vortex cores (of both signs) throughout the boundary layer, attaining a peak at $y^+ \approx 25$ and decaying approximately as $1/(y^+)^{3/4}$ for $y^+ > 50$. For the quasi-streamwise structures, the population of clockwise and counterclockwise cores is very nearly the same, owing to homogeneity in the spanwise direction. Spanwise cores are found to be less numerous than streamwise cores and to be more frequently clockwise (i.e. of the same sign as the mean shear) than counterclockwise, and their number decreases as $1/(y^+)^{1/2}$. In the outer layer, the number densities of the clockwise and counterclockwise spanwise cores and of the streamwise cores (of both signs) are approximately in the ratio 3 : 2 : 4. The computed number densities have very similar magnitude to those reported by Carlier & Stanislas (2005) for low-speed boundary layers. However, those authors found a relatively larger number of spanwise vortices (compared to quasi-streamwise vortices), and reported number densities in the ratio 4 : 2 : 2.

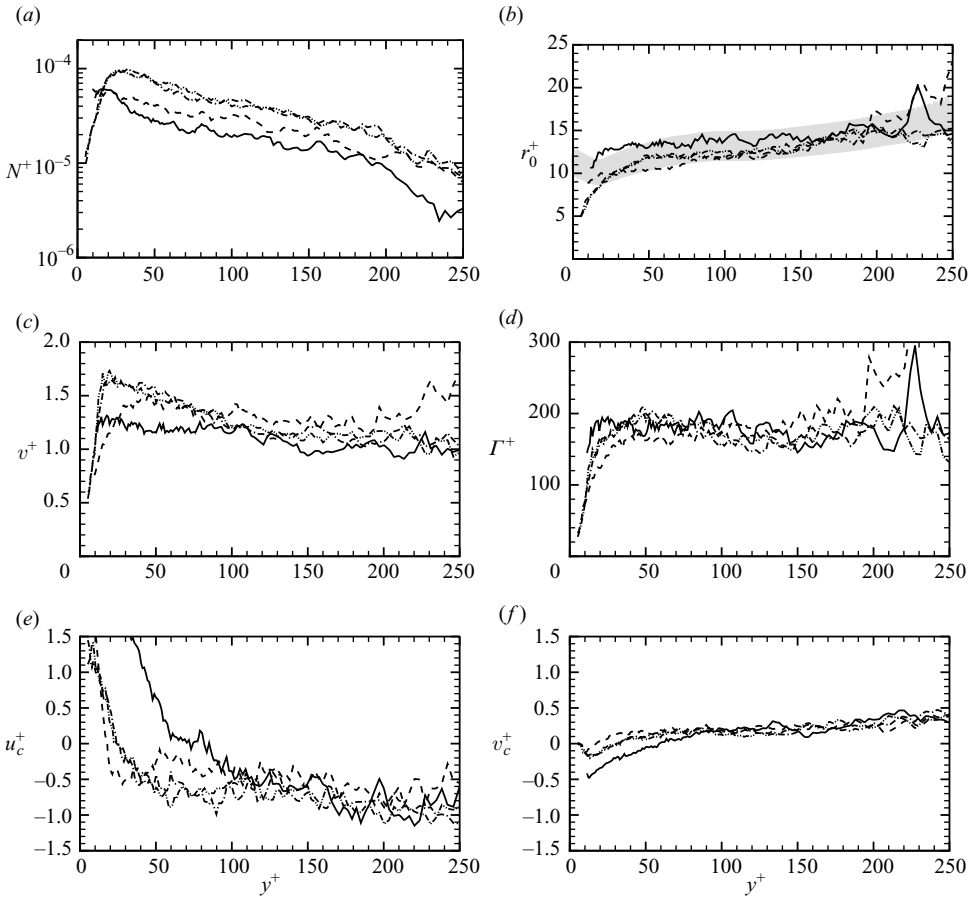

FIGURE 15. Distribution of average vortex core properties as a function of wall distance. (*a*) Number density; (*b*) core radius; (*c*) vortex-induced velocity; (*d*) total circulation (*e*) streamwise convection velocity; (*f*) wall-normal convection velocity. – – –, clockwise spanwise cores; ——, counterclockwise spanwise cores; –·–·–, clockwise quasi-streamwise cores; - · -, counterclockwise quasi-streamwise cores. The shaded area marks the region where $5 < r_0/\eta < 6$.

The distributions of the expected vortex radii of both spanwise and streamwise vortex cores (figure 15*b*) show a rapid increase up to $y^+ \approx 50$. In the outer layer, cores of all types have comparable sizes ($r_0^+ \approx 12$–15). The latter values are consistent with the data reported by Blackwelder & Eckelmann (1979) for streamwise cores, but are somewhat smaller than those reported by Carlier & Stanislas (2005), who found core radii varying between $r_0^+ = 20$ (at $Re_\theta = 7500$) and $r_0^+ = 25$ (at $Re_\theta = 19\,000$). When normalized by the local dissipative length scale, the core radii vary between $5\,\eta$ and $6\,\eta$, in close agreement with the findings of Del Álamo *et al.* (2006).

The vortex-induced velocity (figure 15*c*) exhibits a slow decay with the wall distance, and attains values of $O(u_\tau)$ in the outer region, thus confirming that the commonly assumed turbulent velocity scale (u_τ) is closely associated with the velocity induced by the vortical structures. The mean circulation (figure 15*d*) increases rapidly with the wall distance up to $y^+ \approx 20$, attaining a plateau value of $\Gamma_\infty^+ \approx 180$ in the outer region. This behaviour is consistent with the results of Carlier & Stanislas (2005) (however, those authors report an asymptotic value $\Gamma_\infty^+ \approx 250$), and with the DNS

analysis of Robinson (1991*b*) (who reported $\Gamma_\infty^+ \approx 130$ for quasi-streamwise cores and $\Gamma_\infty^+ \approx 190$ for spanwise cores). The analysis thus indicates that in the outer layer the majority of the educed structures have properties that do not depend upon the wall distance, and in this sense they can be classified as detached eddies.

The distributions of the mean streamwise and wall-normal core translation velocity components (reported in figures 15*e* and 15*f*), show that the detected structures propagate in the negative x- and positive y-direction (with respect to the mean flow) at an average speed of the order of the friction velocity. This result is in agreement with the experimental findings of Delo, Kelso & Smits (2004), and with the analysis of Del Álamo *et al.* (2006), who showed that detached vortices are preferentially associated with low-u wakes left behind by larger attached vortex clusters. This is also consistent with the qualitative observation (see figure 2 and related discussion) that vortices are preferentially found in conjunction with low-speed streaks, as inferred from the analysis of many flow fields. However, the same effect was not observed in the experiments of Adrian *et al.* (2000) and Carlier & Stanislas (2005), who reported nearly zero convection velocities of vortical structures with respect to the mean flow.

The analysis of the vortex properties for cores whose axes are not normal to the sampling planes (the figures are omitted for brevity) further confirms the insensitivity of the conditional expected radius and circulation to the local orientation.

4.5. *Statistical interpretation of educed structures*

The results reported in § 4.2 have provided reasonable evidence that, in a statistical sense, properties of coherent vortical structures of wall turbulence, such as the spatial orientation, can be interpreted in terms of an ensemble of identical non-interacting closed-loop vortex filaments inclined at a positive angle with respect to the wall.

In order to characterize the topology of such 'typical' outer-layer structures, we assume that (to a first approximation) they can be described as (zero-thickness) vortex filaments, whose equation is

$$\frac{\mathrm{d}\boldsymbol{x}}{\mathrm{d}s} = \boldsymbol{\tau}, \tag{4.7}$$

where s is the arclength along the filament and $\boldsymbol{\tau}$ is the local tangent unit vector. In order to integrate (4.7), we assume that: (i) the differential arc element is proportional to the probability of the associated projection angle θ_{zx} ($\mathrm{d}s \sim P(\theta_{zx})\,\mathrm{d}\theta_{zx}$); and (ii) the elevation and projection angles are related according to $\theta_e = \overline{\theta}_e(\theta_{zx})$.

Referring to figure 16, we express $\boldsymbol{\tau}$ in terms of the local elevation and projection angles, i.e.

$$\boldsymbol{\tau} = (\cos\theta_e\ \sin\theta_{zx},\ \sin\theta_e,\ \cos\theta_e\cos\theta_{zx}),$$

thus obtaining

$$\left.\begin{aligned} \frac{\mathrm{d}x}{\mathrm{d}\theta_{zx}} &= \cos\overline{\theta}_e(\theta_{zx})\ \sin\theta_{zx}\ P(\theta_{zx}),\\ \frac{\mathrm{d}y}{\mathrm{d}\theta_{zx}} &= \sin\overline{\theta}_e(\theta_{zx})\ P(\theta_{zx}),\\ \frac{\mathrm{d}z}{\mathrm{d}\theta_{zx}} &= \cos\overline{\theta}_e(\theta_{zx})\ \cos\theta_{zx}\ P(\theta_{zx}). \end{aligned}\right\} \tag{4.8}$$

Then, using the conditional expected elevation angle and the p.d.f. determined from the DNS data (reported in figure 8), (4.8) is numerically integrated with respect to θ_{zx} from $-\pi$ to π. As anticipated in § 4.2, the resulting curve exhibits a closed-loop shape (an indication of the occurrence of both positive and negative vorticity events), with

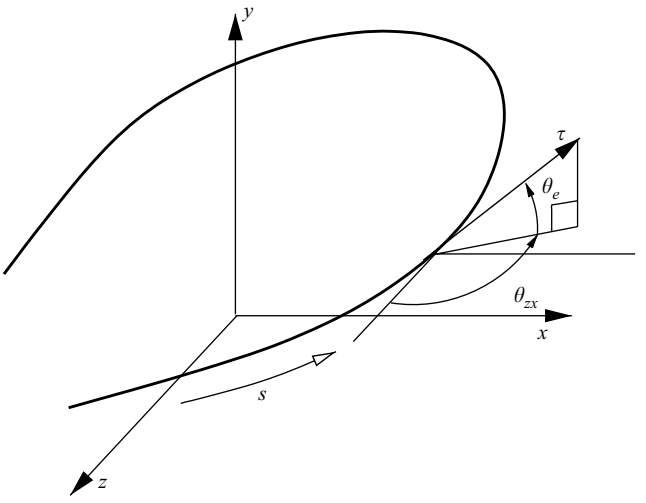

FIGURE 16. Sketch of model vortex filament.

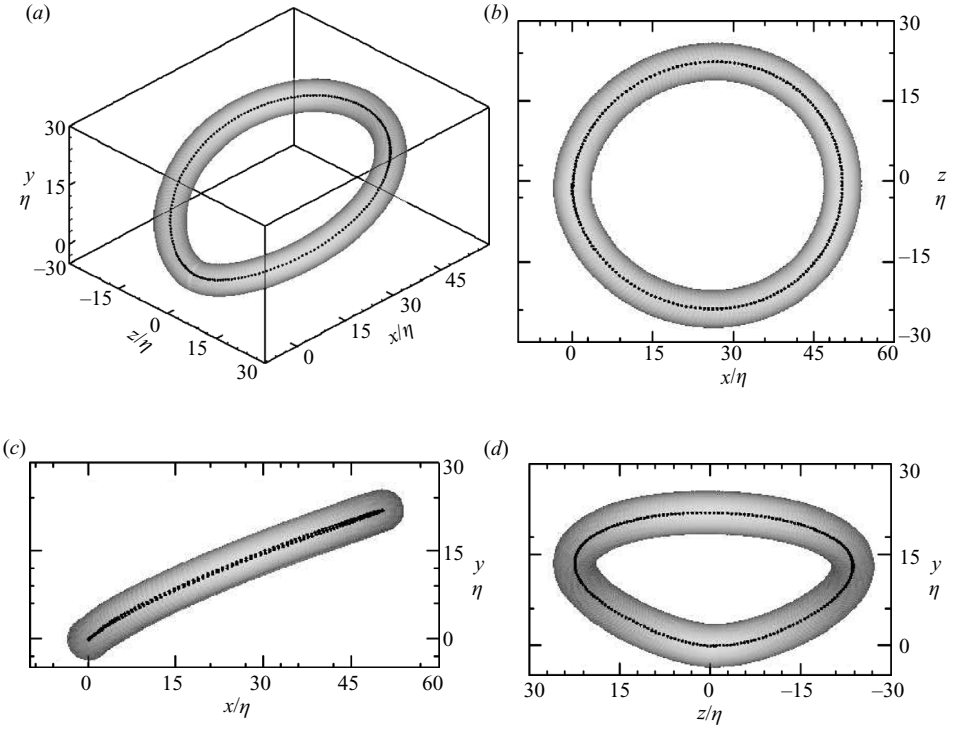

FIGURE 17. Model of statistically educed vortical structure in outer-layer. Black dots indicate points of vortex filament computed according to (4.8) using the $\boldsymbol{\omega}$-criterion. Lengths are reported for indicative purposes in terms of the local dissipative length scale η. (*a*) Three-dimensional view; (*b*) (x, z)-projection; (*c*) (x, y)-projection; (*d*) (y, z)-projection.

a nearly planar head inclined at 20° with respect to the wall (see figure 17). The aft part of the filament is more inclined with respect to the wall (see figure 17*c*), and the radius of curvature at the tail appears to be less than the corresponding value at the

head. The latter observation is consistent (see figure 15(*a*) and associated discussion) with the observed disparity in the number density of spanwise cores with positive and negative spanwise vorticity. With regard to the length scales of the statistically representative outer-layer structures, from figures 12 and 15(*b*) we infer that they have a characteristic overall size (assuming it is of the order of the local radius of curvature of the vortex lines) of 27–35 η and a core radius of 5–6η, consistent with the findings of Del Álamo *et al.* (2006) for the features of detached vortex clusters in incompressible channel flow.

The model here developed provides a theoretical basis for the statistical interpretation of the outer-layer structures, and it supports the conclusions of the various investigators who have associated the occurrence of positive vorticity events with the presence of closed-loop vortex structures. Klewicki & Falco (1990) pointed out that in the very near-wall layer ($y^+ < 10$) the instantaneous spanwise vorticity (ω_z) is always negative. Further away from the wall, they found a relatively high probability (40 % at $y^+ = 40$) of positive spanwise vorticity events, an indication that locally closed vortex loops are possible. Klewicki (1997) further suggested that the near-wall layer can be regarded as a sheet-like vorticity distribution which acts as a source for the generation of compact vortical structures. The analysis of two-point vorticity correlations also led the author to the conclusion that positive and negative vorticity regions often come in pairs, thus supporting the existence of ring-like structures (the 'typical-eddies' proposed by Falco 1977). The presence of head vortices with circulation opposite to the mean shear was also recognized by Kline & Portela (1997); however, no physical explanation was given by those authors to justify the occurrence of counterclockwise cores. Hambleton, Hutchins & Marušić (2006) have observed both negative and positive spanwise vorticity events in the outer layer, and argued that they are due either to omega-shaped vortex loops, or possibly to vortex rings.

With regard to the issue of how closed-loop structures form, we argue that the inner-layer positive-vorticity events may trigger an inflectional instability mechanism, as also proposed by Acarlar & Smith (1986) and Klewicki (1997). Inner-layer structures are subsequently shed away from the wall, maintaining their properties (in terms of size, strength and orientation) while undergoing a slow decay process owing to molecular diffusion. Such a mechanism also explains the observed insensitivity of all vortex properties to wall distance and local core orientation.

5. Conclusions

In the present study, a canonical supersonic boundary layer at $M = 2$, $Re_\theta = 950$ has been analysed by means of a spatial direct numerical simulation, with the objective of quantitatively characterizing the coherent vortical structures in terms of their size and orientation. The study, while being limited to a single Mach and Reynolds number, supports the well-established similarities between compressible (for M less than about 5) and incompressible turbulent boundary layers for the mean and statistical properties, embodied by Morkovin's hypothesis. In addition, it also supports similarities in the observed features of coherent vortical structures (length scales, orientation and strength). In particular, the analysis shows that the viscous sublayer and the buffer layer (collectively referred to as the inner layer) are mostly populated by quasi-streamwise vortices with small inclination with respect to the wall, and which attain a peak number density at $y^+ \approx 25$. The logarithmic layer and the wake region (collectively referred to as the outer layer) are populated by a variety

of structures: elongated quasi-streamwise vortices, arches, a few inverted arches, and hairpin vortices (either isolated or arranged in packets).

In the outer region ($y^+ > 40$), the number density of the educed structures decays algebraically with the distance from the wall, and the number density of clockwise and counterclockwise spanwise cores and streamwise cores (of either sign) are approximately in the ratio 3 : 2 : 4. The size of the educed structures grows with the distance from the wall in the inner layer ($y^+ < 40$), and it levels off in the outer layer where it attains values ranging from 5 to 6 local dissipative length scales. The circulation of the vortices does not show significant variations with the distance from the wall in the outer region, attaining a value of $\Gamma^+ \approx 180$, regardless of the local vortex orientation. The educed structures move (with respect to the mean flow) in the negative x- and positive y-directions at a speed of the order of the friction velocity, and induce velocity perturbations of the same order of magnitude; their properties vary slowly with the distance from the wall and, according to Townsend's classification, they are detached from the wall.

Assuming that the outer-layer turbulence consists of an ensemble of geometrically identical non-interacting vortices, the simulation shows that the statistically representative outer-layer structures are ring-like vortices inclined at approximately 20° with respect to the wall plane. Such a value has been determined upon inspection of the statistical relation between the elevation angle and the projection angle in the wall plane, and it represents a statistical average inclination of all vortical structures, including quasi-streamwise vortices and hairpins. The overall size of the typical structures is found to be approximately 27–35 dissipative length scales, consistent with the scaling obtained by Del Álamo *et al.* (2006) for detached vortex clusters in incompressible channel flow. The finding that ring-like vortices are the statistically representative outer-layer structures is consistent with the presence of open-loop vortices (both quasi-streamwise vortices and hairpins) in the instantaneous fields, and may provide a physical interpretation for the occurrence of both positive and negative spanwise vorticity events.

We acknowledge the CASPUR computing consortium of the University of Rome 'La Sapienza' for providing the computational resources to perform the direct numerical simulation; we specially thank Michela Botti for her support in the parallelization and optimization of the code.

REFERENCES

Acarlar, M. S. & Smith, C. R. 1986 A study of hairpin vortices in a laminar boundary layer. Part 1. Hairpin vortices generated by a hemisphere protuberance. *J. Fluid Mech.* **175**, 1–41.

Adrian, R. J., Meinhart, C. D. & Tomkins, C. D. 2000 Vortex organization in the outer region of the turbulent boundary layer. *J. Fluid Mech.* **422**, 1–54.

del Álamo, J. C. & Jiménez, J. 2003 Spectra of the very large anisotropic scales in turbulent channels. *Phys. Fluids* **15**, L41–L44.

del Álamo, J. C., Jiménez, J., Zandonade, P. & Moser, R. D. 2006 Self-similar vortex clusters in the turbulent logarithmic region. *J. Fluid Mech.* **561**, 329–358.

Blackwelder, R. F. & Eckelmann, H. 1979 Streamwise vortices associated with the bursting phenomenon. *J. Fluid Mech.* **94**, 577–594.

Carlier, J. & Stanislas, M. 2005 Experimental study of eddy structures in a turbulent boundary layer using particle image velocimetry. *J. Fluid Mech.* **535**, 143–188.

Chakraborty, P., Balachandar, S. & Adrian, R. J. 2005 On the relationships between local vortex identification schemes. *J. Fluid Mech.* **535**, 189–214.

Chernyshenko, S. I. & Baig, M. F. 2005 The mechanism of streak formation in near-wall turbulence. *J. Fluid Mech.* **544**, 99–131.

Chong, M. S., Soria, J., Perry, E., Chacin, J., Cantwell, B. J. & Na, Y. 1998 Turbulence structures of wall-bounded shear flows found using DNS data. *J. Fluid Mech.* **357**, 225–247.

Chong, M. S., Perry, A. E. & Cantwell, B. J. 1990 A general classification of three-dimensional flow fields. *Phys. Fluids* A **2**, 765–777.

Delo, R. M., Kelso, C. J. & Smits, A. J. 2004 Three-dimensional structure of a low-Reynolds-number turbulent boundary layer. *J. Fluid Mech.* **512**, 47–83.

Eléna, M. & Lacharme, J. 1988 Experimental study of a supersonic turbulent boundary layer using a laser Doppler anemometer. *J. Méc. Théor. Appl.* **7**, 175–190.

Falco, R. E. 1977 Coherent motions in the outer region of turbulent boundary layers. *Phys. Fluids* **20**, S124–S132.

Farin, G. 1992 *Curves and Surfaces for Computer Aided Geometric Design*. Academic.

Ganapathisubramani, B., Longmire, E. K. & Marušić, I. 2006 Experimental investigation of vortex properties in a turbulent boundary layer. *Phys. Fluids* **18**, 055105.

Gatski, T. B. & Erlebacher, G. 2002 Numerical simulation of a spatially evolving supersonic turbulent boundary layer. *NASA TM* 211934.

Guarini, S. E., Moser, R. D., Shariff, K. & Wray, A. 2000 Direct numerical simulation of a supersonic boundary layer at Mach 2.5. *J. Fluid Mech.* **414**, 1–33.

Hambleton, W. T., Hutchins, N. & Marušić, I. 2006 Simultaneous orthogonal-plane particle image velocimetry measurements in a turbulent boundary layer. *J. Fluid Mech.* **560**, 53–64.

Hamilton, J. M., Kim, J. & Waleffe, F. 1995 Regeneration mechanisms of near-wall turbulent structures. *J. Fluid Mech.* **287**, 317–348.

Head, M. & Bandyopadhyay, P. 1981 New aspects of turbulent boundary-layer structure. *J. Fluid Mech.* **107**, 297–338.

Hutchins, N., Hambleton, W. T. & Marušić, I. 2005 Inclined cross-stream stereo particle image velocimetry measurements in turbulent boundary layers. *J. Fluid Mech.* **541**, 21–54.

Jiménez, J. & Pinelli, A. 1999 The autonomous cycle of near-wall turbulence. *J. Fluid Mech.* **389**, 335–359.

Kim, H. T., Kline, S. J. & Reynolds, W. C. 1971 The production of turbulence near a smoth wall in a turbulent boundary layer. *J. Fluid Mech.* **50**, 133–160.

Klewicki, J. C. 1997 Self-sustaining traits of near-wall motions underlying boundary layer stress transport. In *Self-sustaining Mechanisms of Wall Turbulence* (ed. R. L. Panton), vol. 15, pp. 135–166. Computational Mechanics.

Klewicki, J. C. & Falco, R. E. 1990 On accurately measuring statistics associated with small-scale structure in a turbulent boundary layers using hot-wire probes. *J. Fluid Mech.* **219**, 119–142.

Kline, S. J. & Portela, L. M. 1997 A view of the structure of turbulent boundary layers. In *Self-Sustaining Mechanisms of Wall Turbulence* (ed. R. L. Panton), vol. 15, pp. 167–180. Computational Mechanics.

Kline, S. J., Reynolds, W. C., Schraub, W. C. & Runstadler, F. A. 1967 The structure of turbulent boundary layers. *J. Fluid Mech.* **30**, 741–773.

Li, Q. & Coleman, G. N. 2003 DNS of an oblique shock wave impinging upon a turbulent boundar layer. In *Direct and Large-Eddy Simulation V (ERCOFTAC Series 9)* (ed. R. Friedrich, B. J. Geurts & O. Metais), pp. 387–396. Kluwer.

Maeder, T., Adams, N. A. & Kleiser, L. 2001 Direct simulation of turbulent supersonic boundary layers by an extended temporal approach. *J. Fluid Mech.* **429**, 187–216.

Martin, M. P. 2004 DNS of hypersonic turbulent boundary layers. *AIAA Paper* 04-2337.

Marušić, I. & Perry, A. E. 1995 A wall-wake model for the turbulence structure of boundary layers. Part 2. Further experimental support. *J. Fluid Mech.* **298**, 389–407.

Morkovin, M. V. 1961 Effects of compressibility on turbulent flows. In *Mécanique de la Turbulence*, p. 367. A. Favre (CNRS, Paris).

Ong, L. & Wallace, J. M. 1998 Joint probability density analysis of the structure and dynamics of the vorticity field of a turbulent boundary layer. *J. Fluid Mech.* **367**, 291–328.

Perry, A. E. & Chong, M. S. 1982 On the mechanism of wall turbulence. *J. Fluid Mech.* **119**, 173–217.

Perry, A. E. & Marušić, I. 1995 A wall-wake model for the turbulence structure of boundary layers. Part 1. Extension of the attached eddy hypothesis. *J. Fluid Mech.* **298**, 361–388.

Pirozzoli, S. & Grasso, F. 2004 Direct numerical simulations of isotropic compressible turbulence: influence of compressibility on dynamics and structures. *Phys. Fluids* **16** (12), 4386–4407.

Pirozzoli, S. & Grasso, F. 2006 Direct numerical simulation of impinging shock wave turbulent boundary layer interaction at $m = 2.25$. *Phys. Fluids* **18**, 065113.

Pirozzoli, S., Grasso, F. & Gatski, T. B. 2004 Direct numerical simulation and analysis of a spatially evolving supersonic turbulent boundary layer at $M = 2.25$. *Phys. Fluids* **16** (3), 530–545.

Ringuette, M. J., Wu, M. & Martin, M. P. 2008 Coherent structures in direct numerical simulation of turbulent boundary layers at Mach 3. *J. Fluid Mech.* **594**, 59–69.

Robinson, S. K. 1989 Space–time correlation measurements in a compressible turbulent boundary layer. *AIAA Paper* 86-1130.

Robinson, S. K. 1991*a* Coherent motions in the turbulent boundary layer. *Annu. Rev. Fluid Mech.* **23**, 601–639.

Robinson, S. K. 1991*b* The kinematics of turbulent boundary layer structure. *NASA TM* 103859.

Robinson, S. K., Kline, S. J. & Spalart, P. R. 1989 A review of quasi-coherent structures in a numerically simulated boundary layer. *NASA TM* 102191.

Sandham, N. D., Yao, Y. F. & Lawal, A. A. 2003 Large-eddy simulation of transonic flow over a bump. *Intl J. Heat Fluid Flow* **24**, 584–595.

Smits, A. J. & Dussauge, J. P. 2006 *Turbulent Shear Layers in Supersonic Flow*. American Institute of Physics, New York.

Spalart, P. R. 1988 Direct numerical simulation of a turbulent boundary layer up to $Re_\theta = 1410$. *J. Fluid Mech.* **187**, 61–98.

Spina, E. F. & Smits, A. J. 1987 Organized structures in a compressible turbulent boundary layer. *J. Fluid Mech.* **182**, 85–109.

Spina, E. F., Donovan, J. F. & Smits, A. J. 1991 On the structure of high-Reynolds-number supersonic turbulent boundary layers. *J. Fluid Mech.* **222**, 293–327.

Spina, E. F., Smits, A. J. & Robinson, S. K. 1994 The physics of supersonic turbulent boundary layers. *Annu. Rev. Fluid Mech.* **26**, 287–319.

Theodorsen, T. 1952 Mechanism of turbulence. In *Proc. Second Midwestern Conf. on Fluid Mechanics*, *March, Ohio State Univerisity, Columbus, Ohio*, pp. 17–19.

Townsend, A. A. 1976 *The Structure of Turbulent Shear Flow*, 2nd edn. Cambridge University Press.

White, F. M. 1974 *Viscous Fluid Flow*. McGraw–Hill.

Zhou, J., Adrian, R. J., Balachandar, S. & Kendall, T. M. 1999 Mechanisms for generating coherent packets of hairpin vortices in channel flow. *J. Fluid Mech.* **387**, 353–396.